Journal of Colloid and Interface Science 673 (2024) 373–385

Contents lists available at ScienceDirect

Journal of Colloid And Interface Science

journal homepage: www.elsevier.com/locate/jcis

Regular Article

Hybrid crystalline bioparticles with nanochannels encapsulating acemannan from *Aloe vera*: Structure and interaction with lipid membranes

Rafael R.M. Madrid [a], Patrick D. Mathews [a,b], Shreya Pramanik [c], Agustín Mangiarotti [c], Rodrigo Fernandes [d], Rosangela Itri [d], Rumiana Dimova [c,*], Omar Mertins [a,*]

[a] Laboratory of Nano Bio Materials (LNBM), Department of Biophysics, Paulista Medical School, Federal University of Sao Paulo, 04023-062 Sao Paulo, Brazil
[b] Institute of Biosciences, Sao Paulo State University, 18618-689 Botucatu, Brazil
[c] Max Planck Institute of Colloids and Interfaces, Science Park Golm, 14476 Potsdam, Germany
[d] Applied Physics Department, Institute of Physics, University of Sao Paulo, 05508-900 Sao Paulo, Brazil

GRAPHICAL ABSTRACT

A hybrid lipid-natural source polysaccharides smart cubosome affords crystalline cubic. to inverse hexagonal phase transition and active membrane disturbances for prolonged. and triggered bioactive delivery.

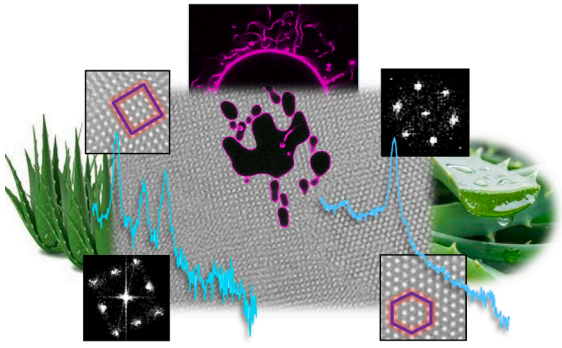

ARTICLE INFO

Keywords:
Smart nanoparticle
Biopolymers complex-coacervates
Liquid crystalline phase transition
Triggered drug delivery
Cubosome-lipid membrane interaction
Cell uptake

ABSTRACT

Smart nanocarrier-based bioactive delivery systems are a current focus in nanomedicine for allowing and boosting diverse disease treatments. In this context, the design of hybrid lipid-polymer particles can provide structure-sensitive features for tailored, triggered, and stimuli-responsive devices. In this work, we introduce hybrid cubosomes that have been surface-modified with a complex of chitosan-*N*-arginine and alginate, making them pH-responsive. We achieved high-efficiency encapsulation of acemannan, a bioactive polysaccharide from *Aloe vera*, within the nanochannels of the bioparticle crystalline structure and demonstrated its controlled release under pH conditions mimicking the gastric and intestinal environments. Furthermore, an acemannan-induced phase transition from Im3m cubic symmetry to inverse hexagonal H_{II} phase enhances the bioactive delivery by compressing the lattice spacing of the cubosome water nanochannels, facilitating the expulsion of the encapsulated solution. We also explored the bioparticle interaction with membranes of varying curvatures, revealing thermodynamically driven affinity towards high-curvature lipid membranes and inducing

* Corresponding authors.
E-mail addresses: Rumiana.Dimova@mpikg.mpg.de (R. Dimova), mertins@unifesp.br (O. Mertins).

https://doi.org/10.1016/j.jcis.2024.06.073
Received 20 April 2024; Received in revised form 5 June 2024; Accepted 7 June 2024
Available online 10 June 2024

morphological transformations in giant unilamellar vesicles. These findings underscore the potential of these structure-responsive, membrane-active smart bioparticles for applications such as pH-triggered drug delivery platforms for the gastrointestinal tract, and as modulators and promoters of cellular internalization.

1. Introduction

Hybrid lipid-polymer nanoparticles are considered an emerging generation of carriers for drugs and bioactives across numerous biological and medical applications [1–3]. These nanoparticles are designed to be systematically engineered into structures that ensure high efficiency in encapsulating bioactive cargos. Their surface properties are tailored for specific interactions with biological targets and the surrounding milieu. Ideally, the encapsulated bioactives should demonstrate attenuated or controlled release kinetics to optimize biological activity.

Cubosomes are liquid crystalline nanoparticles formed through the self-assembly of monoacylglycerol lipids into highly curved lipid bilayers in water. This process leads to the formation of 3D networks with defined and thermodynamically stable crystalline topologies. The intricate aqueous channels within the cubosome structure offer a potentially protective, confined space for water-soluble bioactives [4,5]. In addition, the network-like structure of the cubosomes provides a large internal surface area, which may attain values as high as 400 m^2 per gram of lipid [6].

Dispersions of surface-modified cubosomes have been proposed for specific applications of these nanoparticles with both hydrophilic and hydrophobic properties. For instance, cationic cubosomes, produced with a synthesized lipid bearing a pharmacophoric headgroup, were demonstrated to synergistically improve the in vitro cytotoxicity of the paclitaxel drug on cancer cell lines [7]. Surface charge manipulation is recognized as one of the strategies for designing micro- and nanoparticles with modulated interaction with biological membranes [8–10]. Consequently, lipid particles tailored with charged polymers have been proposed for various biomedical applications, including antibacterial, anticancer, and genetic therapy [11–13]. Regarding cubosomes, surface coating with poly-ε-lysine [14] or hyaluronic acid [15] has been shown to enhance in vitro functionality and targeted drug delivery.

Recently, our group developed hybrid lipid cubosomes with a surface-tailored polyelectrolyte shell composed of the biopolymers chitosan-*N*-arginine (CHarg) and alginate (ALG) [16]. The shell, formed by complex coacervation of the oppositely charged polyelectrolytes, imparts a pH-responsive characteristic to the hybrid cubosomes. This responsiveness arises from the protonation-deprotonation of CHarg and the deionization-ionization of ALG as the suspension transitions from strong acid to alkaline conditions. Furthermore, the hybrid cubosomes effectively interact with serum albumin under simulated gastric and intestinal pH conditions, leading to a thermodynamically driven partial transition of the cubosomes' internal crystalline structure from the original Im3m cubic topology to the Pn3m cubic phase with reduced lattice parameter [17]. This cubic phase transition indicates the expulsion of the cubosome-encapsulated water content. Such pH-responsive interactions of the tailored nanoparticle can be harnessed for oral drug and bioactive delivery in biologically relevant systems.

In the current study, we successfully encapsulated acemannan, the primary bioactive compound derived from *Aloe vera* extract, within hybrid biopolymers-lipid cubosomes. *Aloe vera* is widely recognized as a medicinal plant used for the prevention and treatment of various health conditions, including skin diseases, metabolic and gastrointestinal disorders, cardiovascular diseases, and cancers [18]. The leaves of this plant serve as a source of polysaccharides stored in the mucilaginous reserve parenchyma [19,20]. Among the polysaccharide group, acemannan, a glucomannan β (1,4)-linked glucose chain with acetyl groups, plays a crucial therapeutic role [21].

Previous studies have demonstrated that acemannan possesses antioxidant properties capable of mitigating damage caused by free radicals [22]. Furthermore, acemannan has been shown to stimulate the proliferation of skin cells by activating the AKT/mTOR signaling pathway in fibroblast cells [23]. It also upregulates pro-inflammatory cytokines such as interleukin -6 and -8 [24]. Recognized as a potential immunomodulatory agent, acemannan was described to significantly induce phenotypic maturation of immature dendritic cells and enhance their functionality by increasing allogeneic mixed lymphocyte reaction and interleukin-12 production [25]. The plethora of beneficial activities makes it a valuable component for the healthcare industry, serving as a main ingredient in hydrogels used for treating burn injuries and promoting bone formation in implants [26,27]. Despite its current limited use in nanoparticles, incorporating acemannan into these nanodevices has the potential to improve local and systemic administration, thereby boosting biological activities.

In this study, we examine the encapsulation of acemannan in hybrid cubosomes focusing on the reactivity of the bioparticle's internal crystalline network. Their structural variations are explored as a strategy for developing smart and responsive nanoparticles. The potential application of acemannan-encapsulating bionaonoparticles is assessed through interactions with different model membrane systems, such as nanometer-sized liposomes, under varying temperature and pH conditions mimicking the gastrointestinal environment. Incubation of the cubosomes with giant unilamellar vesicles (GUVs) reveals a variety of morphological changes in the vesicle structure. We evaluate and discuss the bioparticles in terms of their structure and their implication for function on mimetic cell membranes.

2. Materials and methods

2.1. Materials and reagents

The stock solutions of lipid monoolein (1-oleoyl-*rac*-glycerol, 99 %) and Pluronic F127 (99 %) purchased in powder form (Sigma-Aldrich) were prepared in chloroform at concentrations of 200 and 100 mg/mL, respectively. The lipid 1-palmitoyl-2-oleoyl-*sn-glycero*-3-phosphocholine (POPC, 99 %, Avanti Polar Lipids, Birmingham, AL, USA) was dissolved in chloroform at 100 mg/mL (for liposomes) or 1 mg/mL (for GUVs) and the fluorescent dye Abberior STAR 488 NHS ester (Abberior GmbH, Göttingen, Germany) at 0.5 mg/mL in dimethyl sulfoxide. For confocal microscopy, ATTO 647 *N*-DOPE (Sigma Aldrich) was added to a concentration of 0.1 mol% of total lipid. Chitosan-*N*-arginine (CHarg) was synthesized, purified, and characterized as previously described [28] with a degree of deacetylation of 95 %, an average molecular weight (M_W) of 135 kDa, and a yield of 3.5 % of monomers linked with arginine. Alginate (Alg) was from Sigma-Aldrich with M_W 200 kDa and contained 61 % mannuronic acid and 39 % guluronic acid units. CHarg and ALG were individually dissolved in acetate buffer pH 4.5 (40 mM) at 5 mg/mL with overnight stirring followed by 5 min bath sonication. Acemannan BiAloe® in powder extracted from certified organic *Aloe vera* was provided by Lorand Laboratories (Houston, TX, USA) with M_W 17 kDa. Gastric buffer pH 2.5 was prepared with potassium chloride and hydrochloric acid and intestinal buffer pH 7.4 with disodium phosphate and citric acid, both at 80 mM. Sucrose and glucose were purchased from Sigma Aldrich. All reagents were of analytical grade. Purified water was from a MilliQ system (Millipore Corp.) with a resistivity of 18 MΩ/cm and a total organic carbon value under 15 ppb.

2.2. Preparation of bioparticles and liposomes

The cubosome bioparticles with a polymer shell (PS-Cub) were produced in glass vials using 50 mg of monoolein and 3.5 mg of Pluronic F127 (PF127) dissolved in chloroform. For fluorescent samples, an amount of 0.1 mg of Abberior Star 488 was included. The solvents were evaporated under a nitrogen gas stream, producing a film inside the glass vial. For samples with bioactive, acemannan (Ac) was prepared separately dissolved at 20 mg/mL in purified water. 250 μL of Ac solution was added to the monoolein-PF127 film and left to rest for 45 min. Then, 528 μL of chitosan-*N*-arginine and 53 μL of alginate solutions were added, bringing the final volume to 3 mL with the desired buffer pH, namely pH 2.5 or pH 7.4. The mixture was vortexed for 2 min and placed in an ultrasonic bath for 5 min (40 kHz, Eco-Sonics Q3.0L, Brazil). The procedure was repeated 10 times. To remove the free dye used to label the samples for confocal microscopy visualization, the cubosome suspension was centrifuged (5000 rpm, 4 °C, 15 min) in an Amicon Filter Unit and the supernatant was discarded and replaced for buffer. This procedure was repeated twice.

For the production of liposomes, 330 μL of POPC dissolved in chloroform was placed in a glass vessel and the solvent was evaporated under a nitrogen gas stream to create a film inside the glass vessel. Then 1 mL of the different buffers with pH 2.5 or 7.4 were added to individual samples. The liposomes were produced via self-assembly using a tip sonicator (125 W, 10 %, Q125 Sonicator, Qsonica, Newtown, CT, USA) for 10 min in an ice bath.

2.3. Preparation of giant unilamellar vesicles

Giant unilamellar vesicles (GUVs) were prepared via the electroformation method. [29] A POPC lipid stock solution in chloroform (10–20 μL, 1 mg/mL) containing 0.1 mol% ATTO 647 *N*-DOPE was spread on two conductive glass substrates coated with indium tin oxide (ITO, PGO GmbH, Iserlohn, Germany). The lipid films were dried in a desiccator under constant vacuum pumping for around 1 h. A rectangular Teflon frame of 1.6 mm thickness was used as a chamber spacer between the two opposing ITO glass substrates. The coated ITO surfaces acted as electrodes. Approximately 2 mL of 10 mM sucrose solution was introduced into the chamber through a 0.22 μm sterile filter (Millipore). An alternating electric field of 1.5 V (peak-to-peak) and 10 Hz was applied using a function generator (Agilent 33220A 20 MHz function/arbitrary waveform generator) for 1–2 h. After electroformation, the vesicle suspension was carefully transferred to an Eppendorf vial. The vesicles were diluted in an isoosmolar glucose solution (pH 7.0). Osmolarities were adjusted with the osmometer Osmomat 030 (Gonotec, Germany). The samples were used within 2 h.

2.4. Encapsulation efficiency and release

The encapsulation efficiency of acemannan in AcPS-Cub was determined using the centrifugal ultrafiltration method [30]. After a sequence of 10 vortex-sonication procedures described by Mathews et al., [16] the AcPS-Cub was transferred to an Amicon Ultra-15 Centrifugal Filter Unit (MWCO 3 kDa, Millipore Corp., MS, USA) and centrifuged at 25 °C for 50 min at 5000 rpm in a microcentrifuge. The filtrate was collected and measured via spectrophotometry at 196 nm (Ultrospec UV – visible GE 8000). The procedure was performed in triplicate. In parallel, a standard calibration curve was constructed by spectrophotometry of solutions of pure acemannan, dissolved at different concentrations in the same aqueous solution as the particles, corresponding to 6 to 100 % of the concentration included in the cubosomes preparation. The concentration of Ac encapsulated in the cubosomes was calculated using the standardized calibration curve based on absorbance versus concentration [31].

The in vitro release of acemannan from the bioparticle was evaluated by dialysis. After preparation, AcPS-Cub samples were individually dispersed in the mimetic gastric (pH 2.5) and intestinal (pH 7.4) solutions of 3 mL for each condition and subsequently transferred to dialysis bags (nitrocellulose membrane, MWCO 3500, Servapor) previously hydrated in purified water. The filled dialysis bags were left suspended in a beaker containing 100 mL of the corresponding buffer and maintained at 37 °C for 36 h. The systems were continuously stirred at 100 rpm, and an aliquot of 1.5 mL was withdrawn from the beaker at determined intervals (10, 20, and 30 min; 1, 2, 4, 6, 8, 24, 26 and 28 h) and the absorbance measured as described above. The volume in the beaker was kept constant by adding the equivalent buffer solution. The cumulative released concentrations were also calculated using the standardized calibration curves based on absorbance versus concentration obtained for the range of acemannan concentrations dissolved in the same solutions as the bioparticles. The release experiments were performed in triplicate.

To evaluate the release mechanism in both pH conditions, zero-order, Higuchi, and Korsmeyer-Peppas mathematical models were applied, [32] following the respective equations:

$$Q(t) = Q_0 + K_0 t \tag{1}$$

where Q is the amount of acemannan released at time t, Q_0 is the initial acemannan amount, and K_0 is the zero-order release constant,

$$Q(t) = K_H \sqrt{t} \tag{2}$$

where K_H is the release rate constant, and

$$\frac{M(t)}{M_\infty} = K_{KP} t^n \tag{3}$$

where $M(t)/M_\infty$ is the acemannan released fraction at time t, K_{KP} is the release rate constant, and n is the release index. Data were adjusted with linear regression of the initial 8 h release, and the square correlation coefficient (R^2) was acquired [33,34].

2.5. Dynamic light scattering and zeta potential

Dynamic light scattering (DLS) and zeta potential measurements were performed in a Nano-ZS90 Malvern ZetaSizer equipment (Malvern Instruments, UK) operating with a 4 mW HeNe laser at a wavelength of 632.8 nm in a temperature-controlled chamber at 25 °C. Aliquots of liposome or cubosome dispersions were diluted to 1 mL with the corresponding buffer of interest. DLS measurements were made with the samples in folded capillary zeta cells and scattering was acquired at 173°. The autocorrelation function was acquired by exponential spacing of the correlation time. The data analyses were performed with software provided by Malvern. The intensity-weighted size distribution was obtained by fitting data with a discrete Laplace inversion routine. Size determination was made using the Stokes-Einstein relation and the polydispersity was accessed by cumulant analysis of the correlation functions measured by DLS applying the amplitude of the correlation function and the relaxation frequency. The second-order cumulant was used to compute the polydispersity of samples. Each determination was obtained from three consecutive measurements. The colloidal particle size was expressed as hydrodynamic diameter.

Zeta potential was measured in the same chamber using the same instrument and data were acquired performing at least 100 runs per sample. The principle of the measurement is based on laser Doppler velocimetry and the electrophoretic mobility was converted to zeta potential using the Helmholtz Smoluchowski relationship and the data were obtained in mV.

2.6. Cryogenic transmission electron microscopy

Cryogenic transmission electron microscopy (cryo-TEM) was performed at the Brazilian Nanotechnology National Laboratory (LNNano,

CNPEM, Campinas, Brazil). Samples were prepared in a controlled environment with temperature and humidity conditions set at 22 °C and 100 %, respectively, using an automated vitrification system (Vitrobot Mark IV, FEI, Netherlands). A lacey carbon-coated copper grid (TED Pella, Redding, USA) of 300-mesh was employed, being the same submitted to a glow discharge treatment generated by an easiGlow® (Pelco) discharge system with a negative current of 15 mA during 10 s. Following, a 3 μL drop of the sample was deposited on the copper grid and an automatic blotting was performed to dry the excess sample with a negative blotting force. Then, the grid was rapidly plunged into liquid ethane wrapped into a liquid nitrogen environment. Finally, grids were transposed to a grid box in liquid nitrogen, and measurements were made in a Jeol JEM-2100 transmission electron microscope operating at 200 kV. The samples were analyzed under low-dose conditions with the defocus in a range between −2 and −4 μm. The snapshots were acquired with a CMOS F-416 camera using EMMENU software, version 4.0.9.52 (TVIPS, Germany). The obtained photomicrographs were processed employing ImageJ® software to analyze the particle's internal structure with image digital treatment by Fast Fourier Transform (FFT).

2.7. Small-angle X-ray scattering

Small-angle X-ray scattering (SAXS) experiments were performed at the Crystallography Laboratory, Institute of Physics, University of São Paulo (USP, São Paulo, Brazil) in a SAXS set-up with a GeniX 3D copper anode source from Xenocs and a Pilatus 300 k detector [35]. Each sample was introduced in a thin-walled glass capillary tube for X-ray diffraction (2 mm diameter, Charlessupper, Westborough, MA, USA) and measured for 60 min at 21 °C with a sample-detector distance of 0.66 m. The SAXS data were azimuthally integrated and averaged over five consecutive runs. The scattering vector modulus $q = 4\pi\sin\theta/\lambda$, with 2θ being the scattering angle and λ being the X-ray wavelength of 1.548 Å, ranged from 0.026 to 0.260 $Å^{-1}$.

For cubic symmetry determinations, the relation between the lattice parameter a and the spacing, q (hkl) of the diffraction peaks is given by:

$$a = \frac{2\pi}{q(hkl)}\sqrt{h^2 + k^2 + l^2} \quad (4)$$

where (hkl) are the Miller indices of the Bragg reflections corresponding to a given cubic symmetry [36]. By plotting q versus $\sqrt{h^2 + k^2 + l^2}$, where q is the peak position along the scattering vector axis, the slope of the linear fit to the data equals the inverse of the lattice parameter.

2.8. Isothermal titration calorimetry

The isothermal titration calorimetry (ITC) measurements were performed in a VP-ITC micro-calorimeter (MicroCal Inc., Northampton, MA). Initially, the samples were degassed for 5 min under reduced pressure to avoid the interference of air bubbles during measurements. Following the standard procedure, the working cell of 1.4576 mL in volume was filled with 5 mM POPC liposomes in buffer at pH 2.5 and 3 mM POPC liposomes in buffer at pH 7.4. The specific and different POPC concentrations were revealed to be necessary in repeating the experiment several times to obtain the saturation of binding sites in the titration for each pH. One aliquot of 2 μL followed by 27 aliquots of 10 μL of AcPS-Cub suspension containing 45 mM monoolein and dispersed in the respective buffer were injected stepwise into the working cell with a 400 s interval between consecutive injections. The sample cell was constantly stirred at 307 rpm, and the experiments were performed at 37 °C. The corresponding control experiments were also performed, namely, titration of AcPS-Cub-free buffer in the liposome suspension, and titration of AcPS-Cub suspension in the liposome-free buffer, and the obtained heats of dilution were subtracted from the main experiments. The data acquisition and analyses were carried out with Origin software provided by MicroCal. The data fitting was performed by applying the single set of identical binding sites model, as previously described, using a non-linear least square fitting [17].

2.9. Laser scanning confocal microscopy

The POPC giant vesicles and cubosomes were transferred into an observation chamber, which was assembled with two glass coverslips separated by a rubber spacer. The sample was observed with a confocal microscope (Leica TCS SP5) with a 63×, 1.2NA water immersion objective. The fluorescent dyes in the GUVs and the cubosomes were excited with a laser at 633 nm (He-Ne laser) and 488 nm (Argon), and the emission signals were collected around 645 nm and 525 nm for ATTO 647 N and Abberior STAR 488, respectively. The images and time-lapse movies were recorded and analyzed with the Leica Application Suite ×1.6.0 software.

3. Results and discussion

3.1. Colloidal features

The monoolein cubosomes containing the biopolymers chitosan-*N*-arginine and alginate as the polymers shell, referred to as PS-Cub, were initially compared to those encapsulating the acemannan bioactive from *Aloe vera*, denoted as AcPS-Cub. The encapsulation efficiency of acemannan, determined by an independent triplicate procedure of the centrifugal ultrafiltration method, was found to be approximately 92 ± 2 %, indicating a high capability for encapsulating the bioactive in the crystalline bioparticle. Table 1 presents dynamic light scattering results for both samples under acidic and slightly alkaline conditions. It is evidenced that the colloidal characteristics of PS-Cub were not altered by the incorporation of acemannan. In particular, the hydrodynamic diameters ranged from 280 to 296 nm at pH 2.5 and from 662 to 685 nm at pH 7.4, with a relatively higher polydispersity in the acidic solution.

Considering the zeta potential, at low pH, both samples exhibited a neutral to slightly positive surface charge, while at pH 7.4 both samples displayed a mildly negative surface charge. The results affirm the fairly pH-responsive feature of PS-Cub provided by the biopolymers acting as effective polyelectrolytes. At low pH, chitosan is protonated and alginate is neutral, whereas at pH = 7.4, chitosan is predominantly neutral and alginate is negatively charged. This accounts for the observed decrease in zeta potential, along with the expansion of the particles, as previously described [16]. Nevertheless, the inclusion of acemannan in the particles effectively did not alter their hydrodynamic size, surface charge, and pH responsiveness.

3.2. Hybrid bioparticles ultrastructure

The colloidal samples ultrastructure was visualized using cryo-TEM. This technique preserves the structure of the particles under study and enables the analysis of their crystalline organization. Fig. 1 shows representative snapshots of the nanoparticles, highlighting the structural similarities and differences between them.

Fig. 1a shows a cryo-TEM photomicrograph of a plain cubosome produced without biopolymers. The snapshot evidences a sharp cubic

Table 1
Colloidal characteristics of polymer shell-cubosomes (PS-Cub) without and with acemannan (Ac) in acid and alkaline solutions in terms of hydrodynamic diameter (D), polydispersity index (PDI), and zeta potential (at pH 2.5 the zeta potential measurements are within the error limit).

Sample	pH	D (nm)	PDI	Zeta (mV)
PS-Cub	2.5	280 ± 65	0.34	+5 ± 6
AcPS-Cub	2.5	296 ± 58	0.31	+5 ± 6
PS-Cub	7.4	685 ± 107	0.25	−18 ± 6
AcPS-Cub	7.4	662 ± 92	0.27	−14 ± 4

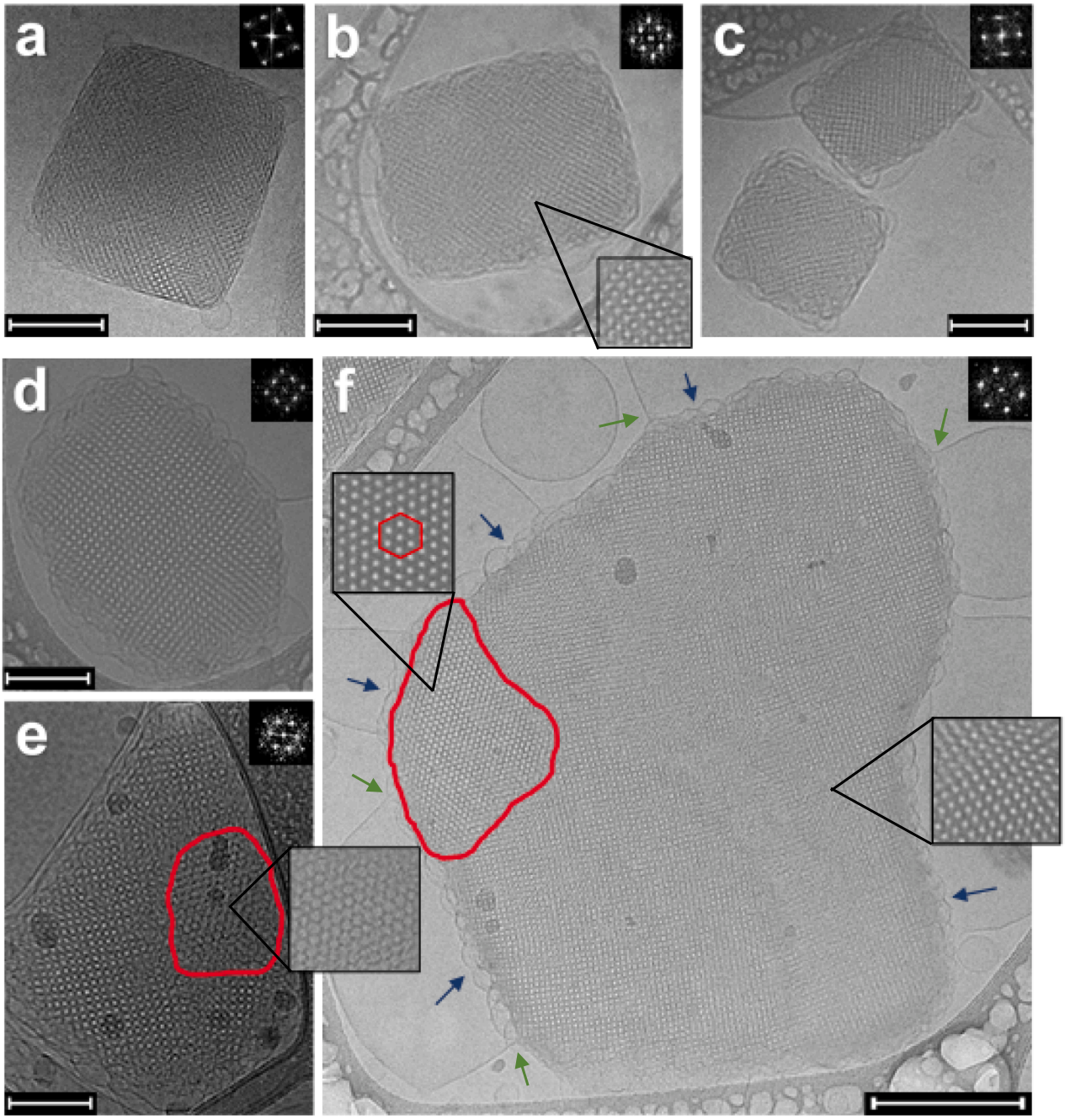

Fig. 1. Cryo-TEM photomicrographs of a plain cubosome without polymer surface functionalization (a), a PS-Cub (b) and two AcPS-Cub (c), all acquired on samples at pH 2.5, and PS-Cub (d) and AcPS-Cub (e,f) acquired on samples at pH 7.4. The insets in the upper right corners show the Fast Fourier Transform (FFT) analysis. The black-framed inserts show amplified regions to better visualize the crystalline patterns. The red hexagonal form and regions delineated in red evidence the hexagonal pattern and the hexagonal phase in specific regions of the AcPS-Cub particles. The blue arrows point to lamellar structures formed at the surface of the particle and protruding as round vesicular caps; some of these structures appear to have fused to form large vesicular protrusions of a few 100 nm height (green arrowheads). All scale bars are 100 nm. (For interpretation of the references to colour in this figure legend, the reader is referred to the web version of this article.)

particle with an internal crystalline pattern, characteristic of monoolein cubosomes of Im3m cubic symmetry [37], as evaluated by FFT (see inset in the upper right corner). Fig. 1b and 1c show a PS-Cub and AcPS-Cub, respectively, with less sharp surfaces evidenced by the presence of lamellar phase surrounding the main external surface of the particles. Nevertheless, it is evidenced that both plain cubosomes and functionalized cubosomes, dispersed in a strong-acidic solution with a pH of 2.5, preserved the internal crystalline structure of Im3m symmetry.

Fig. 1d presents an example of a PS-Cub dispersed in a solution of pH 7.4. Under this condition, cryo-TEM analysis revealed changes in the particle surface, showing an apparent increase in surface lamellarity. While the internal Im3m cubic symmetry was still preserved, a loss of the cubic appearance of the particles and reduced sharpness of the cube edges can be observed.

Remarkably, the AcPS-Cub at pH 7.4 shown in Fig. 1e and f, exhibit distinct structural features. While the surface lamellarity and the reduction of cube edge curvature were still observed, these samples showed a greater variety of particle shapes, concomitant with the formation of larger-size particles. More notably, a marked differentiation in this sample was the presence of an inverse hexagonal (H_{II}) phase, which

additionally modified the particles' internal structure. The regions marked in red in Fig. 1e and f indicate the H_{II} phase, confirmed by the FFT analysis. This shows that these particles undergo a partial phase transition from mainly the Im3m phase to H_{II} upon incorporation of acemannan. This partial phase transition apparently influenced the structure of the whole particle, resulting in particles of different shapes. Note that the particle shown in Fig. 2f exhibits a H_{II} region predominantly in the left corner. This leads to the rest of the structure being bent to the right, suggesting that phase transition changed the particle shape.

Another remarkable observation from the cryo-TEM analysis was that the AcPS-Cub in pH 7.4 presented a softened structure. During imaging, many particles were found lying at the corners of the copper-grid sample support. As shown in Fig. 1e, the particle rests on the right boundary of the grid, adopting the grid curvature. Therefore, we speculate that the inclusion of acemannan induced a certain softening of the cubosomes, presumably providing an increment in the fluidity or deformability of the particles.

Considering the information provided by the cryo-TEM analysis as a whole, it is evident that surface lamellarity on the cubosomes is caused by the biopolymers, which are pH-responsive, leading to surface changes at pH 7.4, as described above. This affirms that the polymer's shell formation influences the curvature of the monoolein lipid bilayers, drastically reducing it and generating surface lamellas of lower curvature. In a study conducted by Demurtas et al. [38], cubosomes produced with glycerol monolinoleate as the main lipid component exhibited surface lamellarity after being heated to 100 °C for 40 min and then cooled down. Membrane fusion events and interlamellar attachments occurred at the particle surface, providing a thick lamellar phase at the particle-water interface. In our samples, such surface characteristics (some indicated by arrows in Fig. 1f) were facilitated by the biopolymers and possibly enhanced by acemannan, without the need for heat treatment. The presence of surface lamellarity on cubosomes can impact at least two important properties for bioactive delivery. One is related to the stability of the particles, as vesicular caps prevent the lipophilic part of the lipid bilayer from coming in contact with water at the water-cubosome interface [38,39], hence influencing the colloidal stability. Additionally, with the surface lamellarity, the cubosome water channels that open to the outside on the particle surface are isolated from the bulk-dispersing water, i.e., the lamellar caps can act as packing covers, thus retarding the release of the encapsulated content. This configuration can influence the release of encapsulated bioactives, especially hydrophilic components such as acemannan, leading to more prolonged or sustained release. The lamellarity effect provided by the biopolymers is apparently highly pronounced at pH 7.4, resulting in the formation of crystalline particles with less sharp corners, as shown. In contrast, for the same particles at pH 2.5, the cubic shape is rather preserved, even in the presence of acemannan from *Aloe vera*.

Furthermore, the remarkable crystalline phase transition from cubic to hexagonal phase can be attributed to the presence of acemannan in the PS-Cub structure when dispersed in a solution of pH 7.4. This transition occurred in a solution of pH 7.4 but not of pH 2.5, indicating the pH-responsive nature provided by the biopolymers under slightly alkaline condition, which further facilitated the phase transition promoted by acemannan. Therefore, a synergistic effect between the biopolymers and acemannan should not be disregarded. The cryo-TEM analysis of the different crystalline structures of the cubosomes was confirmed and further quantitatively analyzed through SAXS, as detailed below.

3.3. Crystalline structure and nanochannels

Fig. 2 shows SAXS curves obtained for the different cubosome samples. The results confirm the crystalline structures observed by cryo-

Table 2
SAXS results for polymer shell-cubosome (PS-Cub) without and with acemannan (Ac) in acid and alkaline solutions in terms of first Bragg peak position (q), respective identified crystalline phase and lattice parameter (a).

Sample	pH	1st q (A^{-1})	Phase	a (nm)
PS-Cub	2.5	0.0592	Im3m	15.3
AcPS-Cub	2.5	0.0572	Im3m	15.5
PS-Cub	7.4	0.0590	Im3m	15.0
AcPS-Cub	7.4	0.0737 – 0.1161	Im3m – H_{II}	12.0 – 5.4

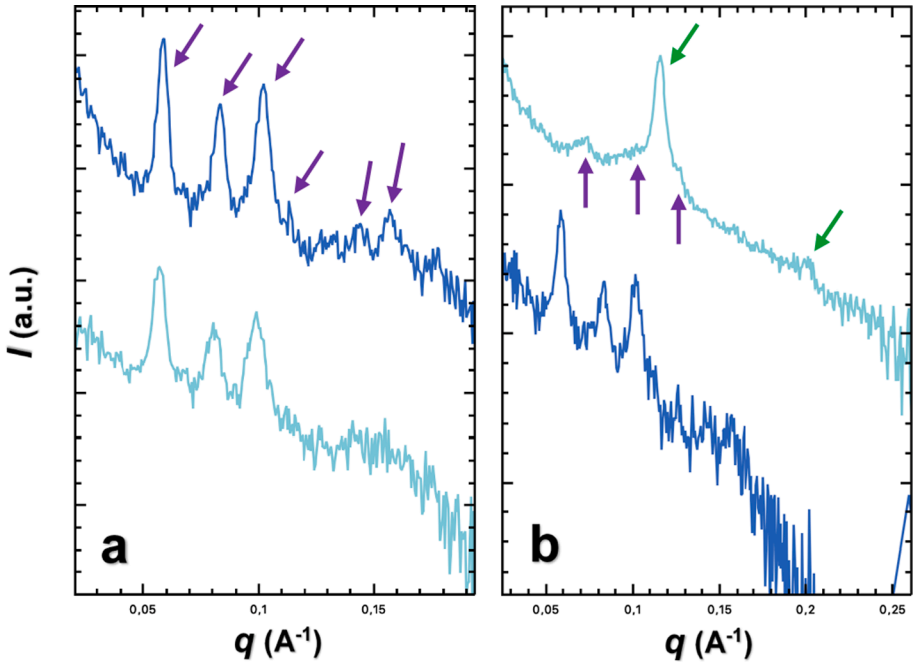

Fig. 2. SAXS patterns correlating intensity (I) with wave vector (q) for PS-Cub (dark blue curves) and AcPS-Cub (light blue curves) dispersed in solutions of pH 2.5 (a) and pH 7.4 (b). Bragg peaks for identified cubic and hexagonal phases are indicated by arrows on the upper curves. See text for more details. (For interpretation of the references to colour in this figure legend, the reader is referred to the web version of this article.)

TEM and additionally provide precise quantitative data and specific topologic phase determination (Table 2). Fig. 2a comparatively shows the SAXS curves for PS-Cub at pH 2.5 without (upper blue curve) and with acemannan (lower light blue curve) evidencing high similarity between these samples. The down-pointing arrows indicate the Bragg reflection peaks with positions spaced in the ratios $\sqrt{2}$: $\sqrt{4}$: $\sqrt{6}$: $\sqrt{8}$: $\sqrt{12}$: $\sqrt{14}$, which index the crystalline cubic phase as corresponding to the Im3m symmetry, equally found for both curves.

Fig. 2b shows the result for PS-Cub particles at pH 7.4 (dark blue curve) exhibiting a similar profile to the samples in acidic conditions, indexing the same Im3m cubic symmetry. However, for the AcPS-Cub upper curve, a noticeably distinct profile emerges. Various Bragg reflections can be identified in this curve, e.g., the up-pointing purple arrows indicate a sequence of three reflections which index in the ratios $\sqrt{2}$: $\sqrt{4}$: $\sqrt{6}$, once again corresponding to the Im3m space group. The two down-pointing green arrows signify the first reflections that correspond to the inverse hexagonal phase (H_{II}) and indexing in the ratio 1: $\sqrt{3}$. The presence of both crystalline phases in the same sample, as evidenced by the SAXS results, confirms the microscopic observations addressed above, corroborating the partial phase transition from cubic to hexagonal phase.

It is worth noting the first Bragg peak position for both samples at pH 2.5 and for PS-Cub at pH 7.4 was nearly identical. Thus, besides the peak indexing confirming the Im3m cubic symmetry, the SAXS analysis also provided the crystalline lattice parameter distances (a) of the internal particle structure (Table 2). As shown, a was also similar and approximately 15 nm, characterizing the internal space of the cubosome bicontinuous aqueous labyrinths for encapsulating bioactives.

At pH 7.4, the AcPS-Cub particles exhibited a noticeable shift in the Bragg reflections in the q range, resulting in a reduction of a from around 15 to 12 nm in the Im3m network. While a reduction of 3 nm may seem minor, when considering the entire particle, it translates to a reduction of 300 nm in distance for every 100 neighboring cubic labyrinths. This implies a squeezing out of the internal aqueous content, leading to structurally highly hydrophobic particles, considering the ratio between the hydrophobic hydrocarbon chains of the lipid and the internal water content. Interestingly, despite this reduction, the overall particle colloidal size was not affected, as shown in Table 1 and with cryo-TEM analysis, revealing even some larger particles nearing one micrometer in diameter. These results suggest the possibility of aggregation and a fusion-like process occurring in AcPS-Cub at pH 7.4, possibly associated with the apparent softening of the particles likely provided by acemannan. In related studies, Rodrigues et al. [40] demonstrated that the presence of acemannan in films made of chitosan and alginate led to increased material flexibility, highlighting the significant influence of acemannan on molecular interactions and moisture enhancements provided by the bioactive, ultimately affecting the structure and mechanical properties of the material.

The prominent hexagonal phase revealed in the corresponding SAXS curve (Fig. 2b) for the same sample is characterized by a sharper and relatively higher intensity Bragg peak compared to the concomitant peaks for the cubic phase (up-pointing arrows). Indexing analysis showed a reduced a value of 5.4 nm (Table 2), indicating an area decrease in the particle internal nanochannels. A similar reduction in a was previously observed in the transition between different cubic phases in chitosan-lipid hydrogel [41]. Thus, the partial transition from cubic to hexagonal phase implicates a significant decrease in the internal crystalline spaces [42], leading to a reduction in the area of the nanochannels and subsequently squeezing out of the aqueous content. The presence of acemannan in the PS-Cub at pH 7.4 promoted a change in the membrane curvature of the monoolein lipid bilayers building the crystalline network. This change involved an increase in the bilayers' negative mean curvature [43], likely due to an expansion of the hydrophobic part of the lipids and/or a reduction of the lipid polar head area, thus enabling the transition to the inverse hexagonal structure [43,44]. As shown, this transition initially reduced the water channels of the cubic phase, decreasing the lattice distance by around 3 nm, followed by a partial transition to the inverse hexagonal phase with higher lipid membrane curvature, further shortening the lattice distance and resulting in a significant reduction of the water channels.

Additionally, the excess increase in membrane curvature in the particle crystalline network may be offset by an increase in particle surface lamellarity, as evidenced by vesicles formation (Fig. 1f), resulting from a drastic reduction of bilayer curvature. Misquitta and Caffrey [45] observed a direct transition from the cubic to the lamellar phase of monoolein cubosome in the presence of high levels of *n*-alkyl-*β*-D-glucopyranosides detergents. The previous research and the present study highlight the influence of various nonionic components on the physical structure of high-viscosity monoolein bilayers, thereby altering the inherent mesophase organization, which can be advantageous for producing smart nanoparticles.

Furthermore, in more complex digestive conditions, it is known that the monoolein lipid is sensible to digestion [46,47]. This is because glyceride lipids possess an ester bond susceptible to lipase enzymes in the gastrointestinal tract. Due to the enzymatic degradation action of lipase enzymes on monoolein, the liquid crystalline structure of bare cubosomes can be disrupted in the digestion medium. In a SAXS study of cubosomes incubated in gastric and intestinal medium containing corresponding enzymes, Nguyen et al. [48] characterized an initial decrease in the cubosome lattice parameter, and after 18 h a transition to non-liquid crystalline inverse micellar (L_2) structures was unveiled. Hence, the digestibility of monoolein can lead the crystalline structure of cubosome to break down, which can be pivotal to providing a specific release profile of encapsulated bioactives [46,48,49]. By contrast, chitosan, which in our study is the main component in the polymer shell over the cubosome surface, cannot be degraded in the stomach or small intestine, being degraded by specific enzymes produced by the colonic microflora [50]. Although our study was performed without lipase enzymes, taking into account the chitosan stability together with the increased lamellarity produced on the bioparticle surface as shown in Fig. 1, we speculate that the biopolymers shell may confer relative protection to the known monoolein degradation in the gastrointestinal tract, hence protecting the cubosome crystalline structure. Indeed, the protection capability of chitosan on lipid-based nano and microparticles has been addressed previously by us and others. [42,51,52] Further studies in simulated digestive mediums will be performed in the future to analyze the stability of the bioparticles to the enzymes.

3.4. Acemannan release from hybrid crystalline bioparticles

Fig. 3 shows the cumulative release of the encapsulated acemannan in the biopolymers-lipid cubosome. The release, performed under simulated gastric and intestinal pH conditions, was attenuated over time. At pH 2.5, a slight initial burst release was observed, reaching an average of 18 % within the first 10 min. The release continued with slightly gradual increases to around 27 % after one hour. The maximum average release achieved at pH 2.5 was 50 %, reached at 6 h of dialysis, and then stabilized.

Contrary to the data at acidic conditions, at pH 7.4, no initial burst was observed and the highly attenuated release during the first 2 h showed reduced and reproducible release percentages (with ratter lower standard deviation), reaching an average of 17 % release in this period. Between 4 and 8 h, there was a higher release, averaging 36 % at 6 h, followed by a further increase after 28 h of dialysis, reaching a maximum average release of 68 %, which then stabilized. From 4 h onwards, there was a notable increase in standard deviation, as shown in Fig. 3. This variation could be associated with the particle's partial internal crystalline phase transition from Im3m cubic symmetry to the inverse hexagonal H_{II} phase, as discussed in the previous section, although long-term time-resolved SAXS experiments could not be performed at this point. The squeezing out of the aqueous content from the crystalline network due to the expressive reduction of lattice parameter

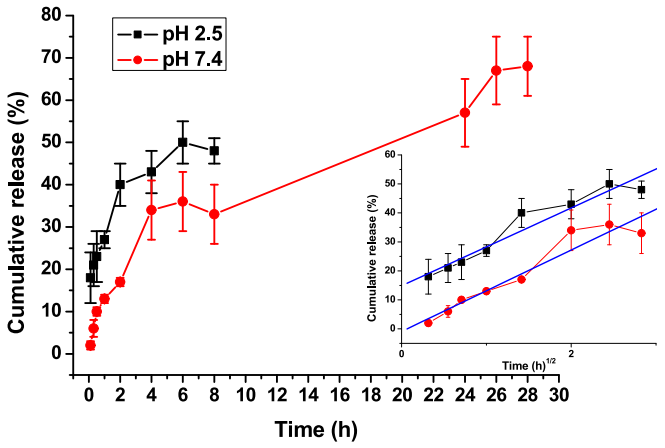

Fig. 3. Cumulative release as a function of time of acemannan from AcPS-Cub bioparticle at 37 °C in simulated gastric (pH 2.5) and intestinal (pH 7.4) conditions. Time zero corresponds to the introduction of the sample in the release media. Error bars correspond to the standard deviation from the average of three independent experiments. Lines are a guide to the eye. The right-inserted graphic plots the same results for the initial 8 h period as the square root of time and shows the corresponding linear regressions, according to the Higuchi release kinetics model.

distances in both Im3m and the resulting H_{II} phase might be responsible for acemannan release at pH 7.4. Despite this, during the first 8 h, the release at pH 7.4 was consistently lower than the release at pH 2.5, on average, indicating the pH-responsive nature provided by the biopolymer shell on the cubosome surface [16]. The initial burst release at pH 2.5 (responsible for the subsequent higher release percentages in gastric conditions) can be attributed to the conformation change of the polymers-shell in the strongly acidic conditions, where despite the maintenance of chitosan-*N*-arginine protonation, alginate loses its negative charge on the carboxyl groups along the macromolecule monomers, resulting in a rather hydrophobic backbone [53]. However, the polymers-shell on the cubosome surface comprises a non-stoichiometric polyelectrolyte complex [28], since a relative excess of chitosan-*N*-arginine was included in the formulation. This excess of the positively charged polymer may have protected the alginate backbone from fast deionization at pH 2.5, prolonging the deionization and leading to a slower conformational change of the polymers-shell entangled network. Hence, during this conformational change of the shell, the cubosome surface may have been highly exposed to the dispersing solution, facilitating aqueous exchanges and boosting acemannan release to 18 %. Such conformational changes of the polymers-shell on the cubosome surface are likely responsible for the initial burst release of acemannan at pH 2.5. Once these conformation changes are complete, a new equilibrium within the biopolymers-shell network is reached, rendering alginate highly hydrophobic. This shell now impedes the aqueous exchanges between the cubosome labyrinths and the exterior, attenuating acemannan release. In a previous SAXS study of the complex coacervates of chitosan-*N*-arginine and alginate in various pH conditions [28], it was shown that in strong acid, the complexes present mass fractal structures with loosely interconnected chains, while in moderately alkaline solutions, a transition from mass to surface fractal occurs, resulting in rough and dense surface where the interface between particles and the aqueous medium is diffuse. Such features of the biopolymers likely further influence the observed release profiles, with the denser macromolecule shell at pH 7.4 better hindering the bioactive release compared to the looser chains at pH 2.5. Notwithstanding, the cumulative release study shows overall a sustained release of acemannan from the PS-cubosome under both gastric and intestinal simulated pH conditions, highlighting its potential for oral delivery applications.

Aiming to compare the mechanism and kinetics of acemannan release from bioparticles in both pHs, the release data for the first 8 h period was analyzed applying Higuchi, zero-order, and Korsmeyer-Peppas models [32–34]. The fit according to the Higuchi model (Fig. 3, insert) provided the most suitable results, with the highest square correlation coefficient $R^2 = 0.9676$ for pH 2.5 and 0.9627 for pH 7.4. By fitting data with zero-order and Korsmeyer-Peppas, the coefficients were around 0.91 (data not shown) and thus no further considered. Higuchi's model (equation (2)) is based on Fick's Law where the release occurs by diffusion and the cumulative released amount is proportional to the square root of time [32]. For this model, the obtained release rate constant $K_H = 13.42 \pm 1.43$ for pH 2.5 and 14.06 ± 1.61 for pH 7.4, thus showing high similarity in both pH conditions. Thereby, the results evidence that the sustained release of acemannan from the bioparticles is controlled by Fickian diffusion in pH 2.5 and 7.4, given the hydrophilic character of the bioactive.

3.5. *Thermodynamic interaction with lipid membranes*

The importance of studying the interactions of new nano or bioparticles with lipid model membranes lies in the fact that cell membranes are predominantly composed and structured by lipid bilayers. Thus, lipid model membranes serve as a valuable tool to evaluate the effects resulting from these interactions, and to predict whether they may perturb cell membranes, potentially leading to endocytosis, or even influencing the apoptosis process [54]. Ultimately, understanding the nature of these interactions can inform the choices of molecules and the proper design of particles, for their intended applications.

In this context, thermodynamic interactions play a crucial role, stemming from physicochemical characteristics such as size, morphology, surface charges, and dispersion conditions. Here, we systematically evaluated the thermodynamics of interaction by applying the same gastric and intestinal simulated pH conditions as for the release experiments and using POPC liposomes as model membranes. By titrating AcPS-Cub in the liposome solution, ITC detects the heat released from the interaction in terms of kcal/mol of monoolein, the cubosome main component, as a function of the molar ratio between monoolein and POPC. Fig. 4 shows the results for both pH conditions, where data fitting (full lines) was achieved by applying the single set of

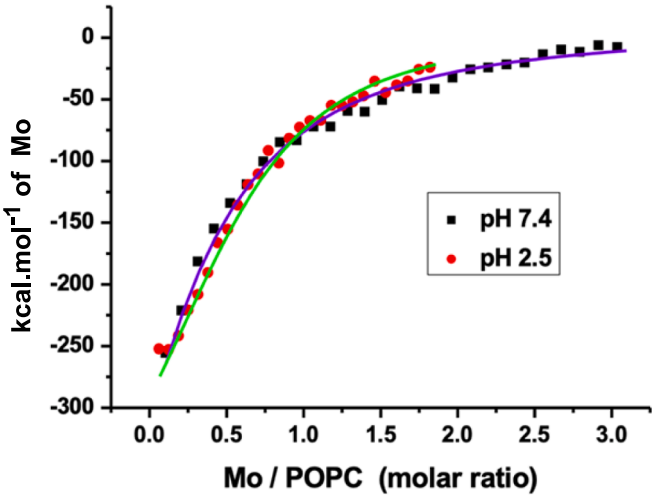

Fig. 4. ITC graph to estimate the heat of interaction and binding constant of the interactions between the cubosomes (AcPS) and the liposomes (POPC) at 37 °C. The experiments are performed at pH 2.5 (red) and pH 7.4 (black) which mimic the gastric and the intestinal surroundings respectively. The solid curves are fitted according to the model for one set of binding sites after subtraction of the heats of dilution. (For interpretation of the references to colour in this figure legend, the reader is referred to the web version of this article.)

binding sites model [17].

The fits in Fig. 4 yielded the thermodynamic parameters characterizing the interactions as presented in Table 3. The number of binding sites N is defined such that $1/N$ represents the number of accessible POPC lipids in the liposome available for binding to monoolein on the cubosome at saturation. At pH 2.5, $1/N$ corresponds to 1.7, and at pH 7.4, to 4.1 on average.

The over two-fold increase in available POPC at pH 7.4 indicates a stronger thermodynamic interaction between AcPS-Cub and liposomes, as corroborated by a higher enthalpy variation of −1.16 kcal/mol on average, compared to the −0.42 kcal/mol in strong acid. This trend is similar to the interaction between the PS-Cub and bovine serum albumin in both pH conditions, as previously described [17]. The binding constant K, was larger at pH 2.5, although on the same order of magnitude as at pH 7.4, indicating effective interacting strength. The exothermic nature of the titration for both conditions, is proof of the favored interaction between AcPS-Cub and POPC, leading to a decrease in Gibbs energy in the order of −6 kcal/mol on average (Table 3).

In addition, the entropic contributions expressed by TΔS evidence a positive entropy variation in both pH conditions, which may be related to conformational changes resulting from the effective interaction. Comparing the colloidal characteristics of the particles before and after the ITC experiment (as shown in Table 4), POPC liposomes presented hydrodynamic diameters around 200 nm and zeta potential values close to neutrality in both pH conditions, as expected for zwitterionic lipid [55], and size polydispersity approximately in the same order as the cubosome particles.

As indicated in Table 4, the colloidal properties changed after titration, leading to structures of new characteristics in terms of size, with an average diameter D of 144 nm at pH 2.5, along with a large increase in polydisperisty (PDI) compared to the individual particles, and three distinct values for zeta potential. Such results suggest possible disruption of liposomes and/or aggregation induced by interaction with the AcPS-Cub, resulting in the formation of a diverse colloidal dispersion with particles exhibiting a wide variety in size distribution and surface charge. Similarly, at pH 7.4, the size distribution revealed two populations of particles along with a high PDI, but surprisingly, a single almost neutral zeta potential. These results indicate severe structural changes resulting from the effective interaction between AcPS-Cub and liposomes, qualitatively describing the obtained entropy increase determined by ITC, which must comprise a result of the sum of structural changes undergone in the interacting particles. Thereby, it is shown that the acemannan-carrying bioparticle effectively interacts with lipid membranes of high curvature as provided by liposomes.

Given the above physicochemical features, it is important to consider the nature of the interaction with caution. As the ITC thermodynamic data reflect the total energy released or absorbed during the interaction, it is not possible to differentiate the individual contributions of different bonds to the total heat [56]. Indeed, the polymers-shell on the surface of cubosome likely plays a crucial role due to the pH-dependent charge distribution and conformation characteristics resulting from hydrophobic and hydrophilic effects [28]. Thus, the polymers-shell leads to the specific energetics described above for the individual acid and slightly alkaline conditions. It is well known that formation of non-covalent bonds (e.g., van der Waals forces, electrostatic interactions or hydrogen bonds) is an exothermic process ($\Delta H < 0$) occurring between hydrophilic surfaces, whereas desolvation, which involves the release of hydration water from the surface of nanoparticles and macromolecules, is usually an endothermic process ($\Delta H > 0$) and can result from surfaces of hydrophobic nature provided by hydrophobic interactions [56].

Furthermore, conformational restrictions and the loss of rotational freedom during particles interactions can lead to a decrease in entropy ($\Delta S < 0$), while the desolvation process may increase it ($\Delta S > 0$) by breaking water hydrogen bonds [57]. Therefore, given the characterized exothermic effect alongside entropy gain resulting from structural alterations of the interacting particles, the different types of interacting processes, i.e., non-covalent bonds, hydrophobic effects, and desolvation describe the complex but effective interaction of the bioparticles with a lipid membrane of high curvature. To qualitatively evaluate this interaction with a membrane of low curvature (characteristic for cell plasma membranes) we utilized giant vesicles, as described below.

Table 3
Results for the thermodynamic parameters characterizing the interaction between AcPS-Cub with POPC liposomes at 37 °C in gastric and intestinal pH conditions as obtained from ITC analysis.

pH	N	K (10^2 M^{-1})	ΔH (kcal/mol)	ΔG (kcal/mol)	TΔS (kcal/mol)
2.5	0.580 ± 0.029	6.06 ± 0.67	−0.42 ± 0.03	−6.42	6.00
7.4	0.243 ± 0.085	4.28 ± 0.56	−1.16 ± 0.44	−6.21	5.05

Number of binding sites, N; binding constant, K; molar enthalpy, ΔH; Gibbs energy, ΔG; entropic contribution, TΔS.

3.6. Effects on giant vesicles

Giant unilamellar vesicles (GUVs) were employed as a simplified model of the cell membrane to assess the interaction with the hybrid bioparticles. Due to lipid protonation, stable vesicles cannot be formed at very low pH. Thus, the interaction and extent of morphological transformations of the GUVs were tested at pH 7.0. Fig. 5 shows a variety of pronounced effects induced on POPC giant vesicles when incubated with cubosomes, whether unloaded (PS-Cub) or loaded with acemannan (AcPS-Cub). As additionally shown in the Supplementary videos, the bioparticles led to large-scale deformations of the giant vesicles, including outward and inward budding, nanotube formation, generation of multiple smaller vesicles from a single larger vesicle, restructuring of the GUVs into ones filled with smaller vesicles encapsulating the original external aqueous content (Video 5).

It is evidenced that the morphology of the GUV membrane undergoes significant perturbation due to the effective interaction with PS-Cub. Comparing PS-Cub (Fig. 5a-c) with acemannan-doped AcPS-Cub under the same conditions (Fig. 5d, e), it becomes apparent that in both cases, the bioparticles induce a rapid increase in GUV area, resulting in large-scale morphological changes. The GUVs in the presence of PS-Cub produce smaller daughter vesicles, which appear as satellites around the mother vesicle (and may remain connected via membrane nanotubes, Fig. 5c, middle image). This significant increase in membrane area indicates the incorporation of material from PS-Cub into the GUVs.

In contrast, for AcPS-Cub, initially, a large amount of nanotubes were observed to form and protrude out of the vesicle membrane (Fig. 5d). Outward nanotube formation may be associated with asymmetric incorporation of material in the bilayer, resulting in expansion of the outer leaflet generating strong positive spontaneous curvature while overall increasing the membrane area. Although the nanotube diameters are below optical resolution, similar examples are provided by the asymmetric insertion of amphiphiles, or ion and macromolecule adsorption [58–61]. However, the membrane nanotubes on GUVs exposed to AcPS-Cub are not stable. After a few minutes, presumably with further insertion of material from the cubosomes, the membrane curvature is inverted to positive, leading to the restructuring of the entire vesicle from a GUV with outward tubes into a vesicle with a large number of smaller inward buds and vesicles (Fig. 5e and Video 5).

We assume that free acemannan, eventually released from the bioparticles, is present only in a negligible amount in the dispersing solution following the centrifugation procedure. Adding supernatant to the GUVs did not produce any detectable changes (data not shown). Alternatively, acemannan encapsulated in the cubosome nanochannels could have been released upon the interaction of the bioparticles with the

Table 4
Hydrodynamic diameter (*D*), polydispersity index (PDI), and zeta potential of the samples of AcPS-Cub and POPC liposome before and after ITC. Data for AcPS-Cub are repeated from Table 1 for better clarity in the discussion.

pH	AcPS-Cub *D* (nm)	PDI	Zeta (mV)	POPC-liposome *D* (nm)	PDI	Zeta (mV)	After ITC (AcPS-Cub + POPC-liposome) *D* (nm)	PDI	Zeta (mV)
2.5	296	0.31	5 ± 6	187	0.35	3 ± 4	144	0.72	−2 (70 %) 16 (19 %) 29 (11 %)
7.4	662	0.27	−14 ± 4	212	0.31	−6 ± 4	429 (66 %) 114 (34 %)	0.54	−1 ± 3

giant vesicle membrane, thus influencing the membrane morphology and leading to the above-described excessive tubulation followed by spontaneous curvature inversion. It is worth noting that in both conditions (PS-Cub and AcPS-Cub), the vesicle membrane preserved stability, and no substances permeated the vesicle interior (as evidenced by the preserved black interior of the GUVs in Fig. 5).

The qualitative evaluation of the bioparticles' interaction with GUVs reveals that they effectively interact and fuse with a lipid membrane of low curvature, such as in GUVs. Interestingly, despite the drastic changes as shown in Fig. 5 and in the Supplementary videos, no vesicle collapse was observed, indicating no membrane rupture or lysis occurred, despite the various types of morphological transformations. Hence, this observation, coupled with the above-described membrane alterations, suggests a highly effective interaction between the hybrid bioparticles and the lipid membrane. This interaction induces both fusion of the bioparticles to the membrane, and external (Fig. 5b,c) and internal (Fig. 5e) budding processes, hence providing means for cell internalization and potential delivery of carried bioactive to cytoplasm.

In a previous study using dioleoylphosphatidylcholine (DOPC), giant vesicles incubated with "bare" monoolein-cubosomes (not stabilized by biopolymers shell) showed various membrane perturbations [62]. The different experimental conditions, including changes in cubosome concentration and the use of different fluorescent dyes, resulted in diverse morphological and topological transitions in giant vesicles, as well as fission and fusion of neighboring vesicles. In our qualitative approach, we observed some of these processes under a single condition for PS-Cub and AcPS-Cub. We witnessed effects resulting from a fusion between particles and vesicle membrane, along with a process resembling phagocytosis, where the particles are encapsulated into smaller vesicles engulfed by the larger vesicles (Fig. 5e).

In a report by Strachan et al. [63], bare cubosomes of monoolein and other lipids were internalized in both murine STO fibroblasts and macrophage cells. The uptake of cubosome in STO fibroblasts was described as mainly due to fusion between the particle and the cell membrane, while in macrophage cells the uptake was preferentially by endocytosis, pointing out that different cell internalizations may occur depending, for instance, on cell type. Additionally, cell uptake of cubosomes occurred after a 3-hour incubation period, a lag time that is not observed in the experiments with giant vesicles. Furthermore, purging out of cubosomes from the cells occurred at later periods.

The varying uptake mechanisms observed in giant vesicles or live cells, as described elsewhere for bare cubosomes and herein for our hybrid bioparticles, underscore the need for further studies to elucidate improvements in composition and engineering aspects. Moreover, they highlight the exceptional prospects of liquid crystalline nanoparticles in applied biomedical fields.

4. Conclusions and perspective

The hybrid crystalline bioparticles, composed of lipid and natural source polysaccharides, exhibit pH-responsive characteristics, which are preserved following the highly efficient encapsulation of acemannan from *Aloe vera*. In strong acidic environments, the biopolymers confer surface lamellarity to the cubic particles, while in slightly alkaline conditions, the particles additionally undergo shape changes while preserving their internal cubic Im3m symmetry. Encapsulated acemannan induces a partial transition from cubic to inverse hexagonal H_{II} phase at pH 7.4. The phase transition significantly shortens the lattice distance, thereby reducing the water nanochannels inside the particles and facilitating the release of aqueous content, representing a mechanism for triggered bioactive delivery. The release of acemannan is gradual and slow, following Fickian diffusion, under simulated gastric and intestinal pH conditions. Moreover, the interaction of the hybrid bioparticles with lipid membranes of high curvature is effective and thermodynamically driven in both acidic and alkaline solutions, resulting in structural changes with an enthalpic decrease but entropy gain. When interacting with low curvature membranes, the bioparticles induce a variety of morphological changes, demonstrating that they can efficiently fuse with the membrane.

In summary, the hybrid crystalline bioparticles hold promise as active transporters of encapsulated content. The encapsulation and delivery of acemannan in smart cubosomes may enhance the application benefits of the *Aloe vera* polysaccharide, particularly in oral applications if intestinal delivery is optimized by the triggering effect. The sustained release and structure-responsive behavior of the bioparticles may boost the immunostimulant and antibody production activities of acemannan, [21] granting improved beneficial effects than the currently commonly used methods to administrate and deliver the bioactive [22,26,40,64]. Further SAXS studies will shed more light on the softening effect of acemannan on the structure of the liquid crystalline bioparticles and their inherent mesophase organization, which can be of great interest in engineering smart nanoparticles.

Furthermore, the bioparticles exhibit promising features as potential natural bioactive delivery systems with effective interactions with lipid membranes, potentially leading to cell membrane modulation, changes in membrane curvature, translocation, and uptake.

CRediT authorship contribution statement

Rafael R.M. Madrid: Writing – original draft, Visualization, Software, Methodology, Investigation, Formal analysis, Data curation. **Patrick D. Mathews:** Writing – original draft, Visualization, Methodology, Investigation, Formal analysis, Data curation. **Shreya Pramanik:** Writing – review & editing, Methodology, Investigation, Data curation. **Agustín Mangiarotti:** Writing – review & editing, Methodology, Investigation, Data curation. **Rodrigo Fernandes:** Software, Methodology, Investigation, Data curation. **Rosangela Itri:** Writing – review & editing, Validation, Resources, Formal analysis. **Rumiana Dimova:** Writing – review & editing, Validation, Formal analysis. **Omar Mertins:** Writing – review & editing, Writing – original draft, Visualization, Validation, Supervision, Resources, Project administration, Investigation, Funding acquisition, Formal analysis, Data curation, Conceptualization.

Declaration of competing interest

The authors declare that they have no known competing financial interests or personal relationships that could have appeared to influence

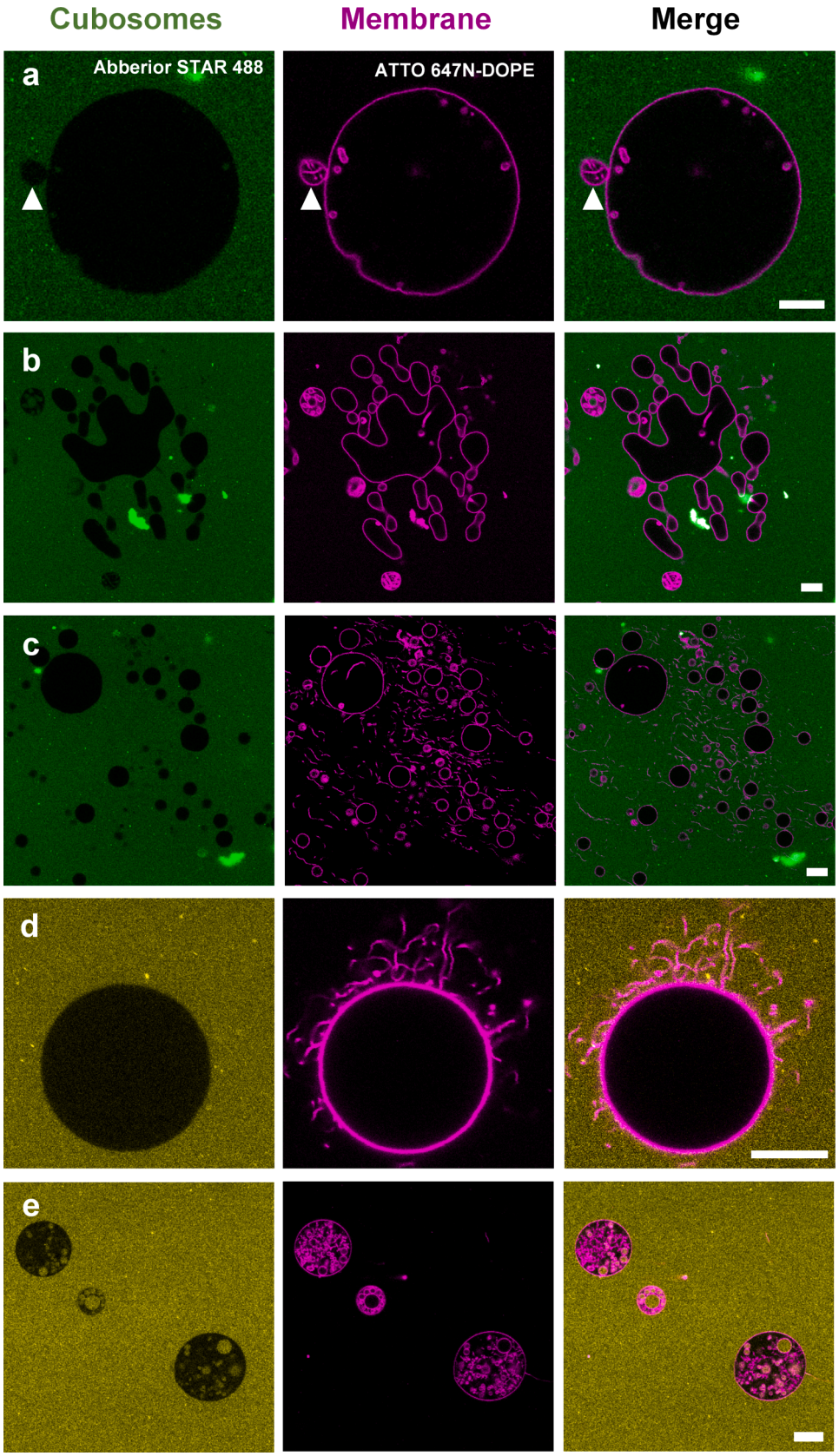

(caption on next page)

Fig. 5. Cubosome-induced membrane morphological transformations over time. PS-Cub suspension without (green) and with (yellow) acemannan in contact with POPC giant vesicles (magenta). The PS-Cub were labeled with 0.5 mol% Abberior STAR 488 and the GUVs membranes contained 0.1 mol% ATTO 647 *N*-DOPE. (a) In the presence of PS-Cub, the vesicles undergo bud formation (white arrowhead). After some minutes, the membranes keep incorporating cubosome material increasing the membrane area and inducing extensive budding and generation of smaller daughter vesicles (b, see Movies 1 and 2). (c) Vesicles recover their sphericity and outward nanotubes are formed (see Movie 3). In the presence of acemannan, when exposed to AcPS-Cub, vesicle tubulation was observed first (d), followed by inward budding (e) (see Movies 4 and 5). Scale bars are 20 μm. (For interpretation of the references to colour in this figure legend, the reader is referred to the web version of this article.)

the work reported in this paper.

Data availability

Data will be made available on request.

Acknowledgments

The authors acknowledge the allocation of cryo-TEM analysis at LNNano (CNPEM, Campinas, Brazil), proposal 20230450, and the kind technical support of Dr. Gisele M.L. Dalmonico. The allocation of SAXS beam time at the Crystallography Laboratory, Institute of Physics, University of Sao Paulo, and the technical support of Dr. Társis Mendes Germano is greatly acknowledged. R.R.M.M. thanks CNPq Brazil for PhD fellowship. O.M. and R.I. also thank CNPq for the research productivity grants. O.M. and P.D.M. thank the Sao Paulo Research Foundation (FAPESP) for research financial support (21/00971-2; 22/12376-4). The Lorand Laboratories is acknowledged for kindly providing the BiAloe® acemannan samples and Prof. Dr. Daniele R. de Araujo is acknowledged for helpful explanation and interpretation of the release mathematical models.

Appendix A. Supplementary data

Supplementary data to this article can be found online at https://doi.org/10.1016/j.jcis.2024.06.073.

References

[1] C. Liu, et al., Extraction, Purification, Structural Characteristics, Biological Activities and Pharmacological Applications of Acemannan, a Polysaccharide from *Aloe vera*: A Review, Molecules 24 (2019) 1554.
[2] A. Mukherjee, et al., Lipid and polymer hybrid nanoparticles as a next-generation drug delivery platform: state of the art, emerging technologies, and perspectives, Int. J. Nanomedicine 14 (2019) 1937–1952.
[3] D. Sivadasan, M.H. Sultan, O. Madkhali, Y. Almoshari, N. Thangavel, Polymeric Lipid Hybrid Nanoparticles (PLNs) as Emerging Drug Delivery Platform—A Comprehensive Review of Their Properties, Preparation Methods, and Therapeutic Applications, Pharmaceutics 13 (2021) 1291.
[4] H.M.G. Barriga, M.N. Holme, M.M. Stevens, Cubosomes: The Next Generation of Smart Lipid Nanoparticles? Angew. Chem. Int. Ed. 58 (2019) 2958–2978.
[5] A.S. Palma, B.R. Casadei, M.C. Lotierzo, R.D. de Castro, L.R.S. Barbosa, A short review on the applicability and use of cubosomes as nanocarriers, Biophys. Rev. 15 (2023) 553–567.
[6] E. Nazaruk, A. Majkowska-Pilip, R. Bilewicz, Lipidic Cubic-Phase Nanoparticles—Cubosomes for Efficient Drug Delivery to Cancer Cells, Chem Plus Chem 82 (2017) 570–575.
[7] S. Pushpa Ragini, et al., Novel bioactive cationic cubosomes enhance the cytotoxic effect of paclitaxel against a paclitaxel resistant prostate cancer cell-line, J. Colloid Interface Sci. 649 (2023) 966–976.
[8] R.R. Arvizo, et al., Effect of Nanoparticle Surface Charge at the Plasma Membrane and Beyond, Nano Lett. 10 (2010) 2543–2548.
[9] V. Forest, J. Pourchez, Preferential binding of positive nanoparticles on cell membranes is due to electrostatic interactions: A too simplistic explanation that does not take into account the nanoparticle protein corona, Mater. Sci. Eng. C 70 (2017) 889–896.
[10] P.D. Mathews, et al., Efficient Treatment of Fish Intestinal Parasites Applying a Membrane-Penetrating Oral Drug Delivery Nanoparticle, ACS Biomater. Sci. Eng. 9 (2023) 2911–2923.
[11] N. Naziris, et al., Biophysical interactions of mixed lipid-polymer nanoparticles incorporating curcumin: Potential as antibacterial agent, Biomater. Adv. 144 (2023) 213200.
[12] G. Wang, et al., Eudragit S100 prepared pH-responsive liposomes-loaded betulinic acid against colorectal cancer in vitro and in vivo, J. Liposome Res. 32 (2022) 250–264.
[13] B.B.M. Garcia, O. Mertins, E.R.D. Silva, P.D. Mathews, S.W. Han, Arginine-modified chitosan complexed with liposome systems for plasmid DNA delivery, Colloids Surf. B Biointerfaces 193 (2020) 111131.
[14] S. Deshpande, et al., Enhancing Cubosome Functionality by Coating with a Single Layer of Poly-ε-lysine, ACS Appl. Mater. Interfaces 6 (2014) 17126–17133.
[15] H. Mun, et al., CD44 and CD221 directed magnetic cubosomes for the targeted delivery of helenalin to rhabdomyosarcoma cells, Nano Res. 16 (2023) 2915–2926.
[16] P.D. Mathews, O. Mertins, B. Angelov, A. Angelova, Cubosomal lipid nanoassemblies with pH-sensitive shells created by biopolymer complexes: A synchrotron SAXS study, J. Colloid Interface Sci. 607 (2022) 440–450.
[17] B.V. Pimenta, et al., Interaction of polyelectrolyte-shell cubosomes with serum albumin for triggering drug release in gastrointestinal cancer, J. Mater. Chem. B 11 (2023) 2490–2503.
[18] Y. Liu, et al., Functional lipid polymeric nanoparticles for oral drug delivery: Rapid mucus penetration and improved cell entry and cellular transport, Nanomedicine Nanotechnol. Biol. Med. 21 (2019) 102075.
[19] C. Luiz, A.C. Da Rocha Neto, P.O. Franco, R.M. Di Piero, Emulsions of essential oils and aloe polysaccharides: Antimicrobial activity and resistance inducer potential against Xanthomonas fragariae, Trop. Plant Pathol. 42 (2017) 370–381.
[20] V.S. Freitas, R.A.F. Rodrigues, F.O.G. Gaspi, Propriedades farmacológicas da Aloe vera (L.), Burm. F. *Rev. Bras. Plantas Med.* 16 (2014) 299–307.
[21] N.J. Sadgrove, M.S.J. Simmonds, Pharmacodynamics of *Aloe vera* and acemannan in therapeutic applications for skin, digestion, and immunomodulation, Phytother. Res. 35 (2021) 6572–6584.
[22] S. Kumar, R. Kumar, Role of acemannan *o*-acetyl group in murine radioprotection, Carbohydr. Polym. 207 (2019) 460–470.
[23] W. Xing, et al., Acemannan accelerates cell proliferation and skin wound healing through AKT/mTOR signaling pathway, J. Dermatol. Sci. 79 (2015) 101–109.
[24] P. Thunyakitpisal, V. Ruangpornvisuti, P. Kengkwasing, J. Chokboribal, P. Sangvanich, Acemannan increases NF-κB/DNA binding and IL-6/-8 expression by selectively binding Toll-like receptor-5 in human gingival fibroblasts, Carbohydr. Polym. 161 (2017) 149–157.
[25] J.K. Lee, et al., Acemannan purified from *Aloe vera* induces phenotypic and functional maturation of immature dendritic cells, Int. Immunopharmacol. 1 (2001) 1275–1284.
[26] Y. Bai, Y. Niu, S. Qin, G. Ma, A New Biomaterial Derived from *Aloe vera*—Acemannan from Basic Studies to Clinical Application, Pharmaceutics 15 (2023) 1913.
[27] P.R. Pachimalla, S.K. Mishra, R. Chowdhary, Evaluation of hydrophilic gel made from Acemannan and Moringa oleifera in enhancing osseointegration of dental implants. A preliminary study in rabbits, J. Oral Biol. Craniofacial Res. 10 (2020) 13–19.
[28] A.C.M.F. Patta, et al., Polyionic complexes of chitosan-*N*-arginine with alginate as pH responsive and mucoadhesive particles for oral drug delivery applications, Int. J. Biol. Macromol. 148 (2020) 550–564.
[29] Dimova, R. & Marques C. *The Giant Vesicle Book*. CRC Press, Boca Raton, FL: CRC Press, Taylor & Francis Group, 2019. Doi:10.1201/9781315152516.
[30] S.J. Wallace, J. Li, R.L. Nation, B.J. Boyd, Drug release from nanomedicines: selection of appropriate encapsulation and release methodology, Drug Deliv. Transl. Res. 2 (2012) 284–292.
[31] R. Delgado, Misuse of Beer-Lambert Law and other calibration curves, R. Soc. Open Sci. 9 (2022) 211103.
[32] P. Costa, J.M.S. Lobo, Modeling and comparison of dissolution profiles, Eur. J. Pharm. Sci. 13 (2001) 123–133.
[33] A.F. Sepulveda, et al., Supramolecular structure organization and rheological properties modulate the performance of hyaluronic acid-loaded thermosensitive hydrogels as drug-delivery systems, J. Colloid Interface Sci. 630 (2023) 328–340.
[34] D. Iudin, et al., Polypeptide Self-Assembled Nanoparticles as Delivery Systems for Polymyxins B and E, Pharmaceutics 12 (2020) 868.
[35] L.M. Furtado, et al., Rheological and mechanical properties of hydroxypropyl methylcellulose-based hydrogels and cryogels controlled by AOT and SDS micelles, J. Colloid Interface Sci. 648 (2023) 604–615.
[36] B. Malheiros, et al., Influence of hexadecylphosphocholine (Miltefosine) in phytantriol-based cubosomes: A structural investigation, Colloids Surf. A Physicochem. Eng. Asp. 632 (2022) 127720.
[37] M. Kluzek, et al., Influence of a pH-sensitive polymer on the structure of monoolein cubosomes, Soft Matter 13 (2017) 7571–7577.
[38] D. Demurtas, et al., Direct visualization of dispersed lipid bicontinuous cubic phases by cryo-electron tomography, Nat. Commun. 6 (2015) 8915.
[39] J. Barauskas, M. Johnsson, F. Joabsson, F. Tiberg, Cubic Phase Nanoparticles (Cubosome): Principles for Controlling Size, Structure, and Stability, Langmuir 21 (2005) 2569–2577.
[40] L.C. Rodrigues, et al., Physicochemical features assessment of acemannan-based ternary blended films for biomedical purposes, Carbohydr. Polym. 257 (2021) 117601.

[41] P.D. Mathews, O. Mertins, Dispersion of chitosan in liquid crystalline lamellar phase: Production of biofriendly hydrogel of nano cubic topology, Carbohydr. Polym. 157 (2017) 850–857.
[42] P.D. Mathews, et al., Flavonoid-Labeled Biopolymer in the Structure of Lipid Membranes to Improve the Applicability of Antioxidant Nanovesicles, Pharmaceutics 16 (2024) 141.
[43] J.M. Seddon, Structure of the inverted hexagonal (HII) phase, and non-lamellar phase transitions of lipids, Biochim. Biophys. Acta BBA - Rev. Biomembr. (1990, 1031,) 1–69.
[44] C. Oliveira, et al., A Versatile Nanocarrier—Cubosomes, Characterization, and Applications, Nanomaterials 12 (2022) 2224.
[45] Y. Misquitta, M. Caffrey, Detergents Destabilize the Cubic Phase of Monoolein: Implications for Membrane Protein Crystallization, Biophys. J. 85 (2003) 3084–3096.
[46] T.H. Nguyen, T. Hanley, C.J.H. Porter, I. Larson, B.J. Boyd, Phytantriol and glyceryl monooleate cubic liquid crystalline phases as sustained-release oral drug delivery systems for poorly water-soluble drugs II. In-vivo evaluation, J. Pharm. Pharmacol. 62 (2010) 856–865.
[47] Warren, D., Anby, M. U., Hawley, A. & Boyd, B. J. Real Time Evolution of Liquid Crystalline Nanostructure during the Digestion of Formulation Lipids Using Synchrotron Small-Angle X-ray Scattering. *Langmuir* **27**, 9528–9534.
[48] T.H. Nguyen, T. Hanley, C.J.H. Porter, B.J. Boyd, Nanostructured liquid crystalline particles provide long duration sustained-release effect for a poorly water soluble drug after oral administration, J. Controll. Rel. 153 (2011) 180–186.
[49] A.C. Phan, T.H. Nguyen, C.J. Nowell, B. Graham, B.J. Boyd, Examining the gastrointestinal transit of lipid-based liquid crystalline systems using whole-animal imaging, Drug Deliv. Transl. Res. 5 (2015) 566–574.
[50] S. Chen, et al., Chitosan-modified lipid nanodrug delivery system for the targeted and responsive treatment of ulcerative colitis, Carbohydr. Polym. 230 (2020) 115613.
[51] O. Mertins, P.D. Mathews, A.B. Gomide, M.S. Baptista, R. Itri, Effective protection of biological membranes against photo-oxidative damage: Polymeric antioxidant forming a protecting shield over the membrane, Biochim. Biophys. Acta Biomembr. 1848 (2015) 2180–2187.
[52] A.C.C. Vieira, et al., Mucoadhesive chitosan-coated solid lipid nanoparticles for better management of tuberculosis, Int. J. Pharmaceutics 536 (2018) 478–485.
[53] A. Haug, B.A. Larsen, B. Samuelsson, J. Sjövall, J. Munch-Petersen, The Solubility of Alginate at Low pH, Acta Chem. Scand. 17 (1963) 1653–1662.
[54] C. Contini, J.W. Hindley, T.J. Macdonald, et al., Size dependency of gold nanoparticles interacting with model membranes, Commun. Chem. 3 (2020) 130.
[55] E. Chibowski, A. Szcześ, Zeta potential and surface charge of DPPC and DOPC liposomes in the presence of PLC enzyme, Adsorption 22 (2016) 755–765.
[56] C. Contini, M. Schneemilch, S. Gaisford, N. Quirke, Nanoparticle–membrane interactions, J. Exp. Nanosci. 13 (2018) 62–81.
[57] K.A.T. Silverstein, A.D.J. Haymet, K.A. Dill, The Strength of Hydrogen Bonds in Liquid Water and Around Nonpolar Solutes, J. Am. Chem. Soc. 122 (2000) 8037–8041.
[58] M. Karimi, et al., Asymmetric Ionic Conditions Generate Large Membrane Curvatures, Nano Lett. 18 (2018) 7816–7821.
[59] Z. Zhao, et al., Super-Resolution Imaging of Highly Curved Membrane Structures in Giant Vesicles Encapsulating Molecular Condensates, Adv. Mater. 34 (2022) 2106633.
[60] R. Dasgupta, M.S. Miettinen, N. Fricke, R. Lipowsky, R. Dimova, The glycolipid GM1 reshapes asymmetric biomembranes and giant vesicles by curvature generation, Proc. Natl. Acad. Sci. 115 (2018) 5756–5761.
[61] B. Ali Doosti, et al., Membrane Tubulation in Lipid Vesicles Triggered by the Local Application of Calcium Ions, Langmuir 33 (2017) 11010–11017.
[62] Xu, Z., Rappolt, M., Tyler, A. & Beales, P. Cubosome-Induced Topological Transformations in Giant Vesicles. Preprint at https://doi.org/10.26434/chemrxiv-2022-6pbbv (2022).
[63] J.B. Strachan, B.P. Dyett, Z. Nasa, C. Valery, C.E. Conn, Toxicity and cellular uptake of lipid nanoparticles of different structure and composition, J. Colloid Interface Sci. 576 (2020) 241–251.
[64] S.A. Im, Y.R. Lee, Y.H. Lee, et al., In vivo evidence of the immunomodulatory activity of orally administered *Aloe vera* gel, Arch. Pharm. Res. 33 (2010) 451–456.